

Correlation between structural and magnetic properties of epitaxial YIG films by pulsed laser deposition

José Diogo Costa^{1,a}, Niels Claessens¹, Giacomo Talmelli¹, Davide Tierno¹, F. Amar², Thibaut Devolder², Matthijn Dekkers³, Florin Ciubotaru¹, and Christoph Adelmann^{1,a}

¹*Imec, 3001 Leuven, Belgium*

²*Université Paris-Saclay, CNRS, Centre de Nanosciences et de Nanotechnologies, 91120 Palaiseau, France*

³*SolMateS BV, Auke Vleerstraat 3, 7521 PE Enschede, The Netherlands*

In this study, we investigate the relationships between film growth conditions, crystalline microstructure, and magnetic properties of epitaxial Yttrium Iron Garnet ($\text{Y}_3\text{Fe}_5\text{O}_{12}$, YIG) thin films, deposited on Gallium Gadolinium Garnet ($\text{Ga}_3\text{Gd}_5\text{O}_{12}$, GGG). A direct correlation was observed between the residual epitaxial strain, bulk magnetic properties like saturation magnetization and magnetic damping), and the performance of spin-wave transmission devices based on these films. This correlation offers a pathway for a simplified, rapid assessment of YIG film quality, avoiding the need for complex time-consuming characterization techniques. In addition, we report a comprehensive investigation into the influence of pulsed-laser deposition parameters, including deposition temperature, pressure, laser fluence, frequency, and annealing conditions. Through systematic deposition optimization, state-of-the-art YIG films exhibiting ultralow magnetic damping could be obtained, which is critical for high-performance spintronic applications.

I. INTRODUCTION

Yttrium Iron Garnet ($\text{Y}_3\text{Fe}_5\text{O}_{12}$, YIG), with its exceptional combination of ultralow magnetic damping, high Curie temperature (560 K), large magnetic permeability, and optical transparency, has garnered substantial interest across various technological domains, in particular for applications in microwave and spintronic technologies.¹⁻⁴ A pivotal factor in realizing the full potential of YIG is however the fabrication of high-quality epitaxial thin films. Epitaxial growth is crucial for attaining the desired magnetic properties and achieving optimal device performance.

^aAuthors to whom correspondence should be addressed. Electronic mail: zediogo.costa@gmail.com and christoph.adelmann@imec.be

Epitaxial thin films of YIG are commonly grown on Gadolinium Gallium Garnet ($\text{Ga}_3\text{Gd}_5\text{O}_{12}$, GGG) substrates owing to the excellent lattice match and the favorable thermal, mechanical, and microwave properties of GGG. Several techniques have been employed for the epitaxial growth of YIG, with Liquid Phase Epitaxy (LPE), sputtering, and Pulsed Laser Deposition (PLD) being the most prominent. LPE facilitates the deposition of high-quality single-crystal films with exceptionally low magnetic damping ($\alpha < 10^{-4}$).^{5,6} However, depositing films thinner than a few hundred nm by LPE presents significant challenges.⁵ By contrast, RF magnetron sputtering, while widely utilized for depositing dielectric films, often results in YIG films exhibiting oxygen vacancies, leading to an increase in magnetic damping ($\alpha \sim 1 \times 10^{-3}$).⁷⁻¹⁰

In contrast, PLD offers exceptional control over film stoichiometry and epitaxy, rendering it highly suitable for depositing complex oxide materials. Notably, ultralow magnetic damping values ($\alpha \sim 10^{-4}$) have been reported for PLD-grown films with thicknesses as low as 20 nm.¹¹⁻²⁰ Several PLD deposition parameters, including deposition temperature, pressure, laser fluence and frequency, as well as annealing conditions, can be systematically adjusted to optimize film deposition. These parameters exert distinct and significant influences on the underlying film formation mechanisms.^{21,22}

For instance, the O partial pressure exerts a significant influence on plume kinetics, enabling the fine-tuning of compositional variations between the target and the deposited film.²³⁻²⁵ However the optimal deposition pressure for achieving the highest film quality remains a subject of ongoing debate. While some studies have reported beneficial effects of higher deposition pressures (up to 0.67 mbar),²⁶ the majority of studies suggest a lower pressure regime (0.01–0.05 mbar) for optimal film growth.^{11,23,27} Laser fluence significantly influences the shape and characteristics of the ablated material plume, impacting both deposition rate and film composition. On the other hand, the frequency of laser pulses determines the time interval available for deposited material to find stable sites before the arrival of subsequent ablated adatoms, affecting adatom thermalization, diffusion, and ultimately the growth mode. However, the combined effects of laser fluence and frequency on the resulting film properties are often under-explored in the literature.²⁶

Growth temperature plays a crucial role by affecting the surface mobility of impinging adatoms and thus the crystal structure and atomic arrangement within the growing film. Reported PLD deposition temperatures for YIG range widely from room temperature to 850°C. While room temperature deposition offers significant advantages

from a processing perspective, *e.g.* by enabling lift-off techniques for subsequent patterning,^{28,29} the majority of high-quality YIG film deposition processes still operate at elevated growth temperatures, typically around 650°C with some variations reported.^{14,19,20,30,31} Even in cases of high-temperature deposition, post-deposition annealing is frequently required to optimize film properties. Annealing in vacuum can lead to oxygen out-diffusion and degrade film quality.³² Therefore, annealing in an oxygen atmosphere is generally preferred to ensure optimal film properties.²³

Hence, there is still a need for a comprehensive understanding of the roles these parameters play in YIG growth. Furthermore, establishing a robust correlation between crystallographic characteristics and material—and ultimately device— performance would significantly expedite the optimization of YIG-based spintronic devices. In this study, we demonstrate a direct correlation between crystal structure and magnetic properties of PLD deposited YIG films, enabling a simplified assessment of magnetic film properties prior to device fabrication. We also elucidate the relationship between deposition conditions and film properties.

As a result, state-of-the-art YIG films with ultralow magnetic damping ($\alpha < 3 \times 10^{-4}$) were achieved under optimized conditions. The optimal deposition conditions, validated at the device level, were determined to be 650°C for deposition temperature, 1.1 J/cm² for laser fluence, 0.04 mbar for O₂ pressure, in combination with post-deposition annealing at 900°C. Furthermore, we also report a strong dependence of YIG properties on film thickness. Notably, as the film thickness increases, the YIG film exhibits a transition from an expanded to a compressed state relative to the lattice parameter of the GGG substrate. This comprehensive understanding of the film growth mechanisms is pivotal for the development of optimized spintronic devices.

II. EXPERIMENTAL DETAILS

All YIG depositions were carried out on (111)-oriented GGG substrates (1" diameter, CrysTec) in a Solmates SIP-800 PLD system.³³ Samples were deposited under a range of deposition conditions, varying systematically temperature (up to 790°C), O₂ pressure, laser fluence, and laser frequency. Subsequently, the films were

annealed post-deposition at various temperatures under an oxygen pressure of 1.8×10^{-2} mbar for 1 hour, using a temperature ramp of 10 K/min for both heating and cooling cycles.

The structural, morphological, and magnetic properties of the YIG films were characterized using x-ray diffraction (XRD, Panalytical X'PERT PRO), scanning transmission electron microscopy (STEM), ferromagnetic resonance (FMR), Rutherford backscattering spectrometry (RBS), and elastic recoil detection analysis (ERD). The film thickness was determined from the Laue oscillations in the XRD spectra and subsequently confirmed through STEM analysis.

Device fabrication was carried out using a combination of hard mask definition and YIG wet etching. The hard mask (30 nm SiO_2) was patterned through CF_4 reactive ion etching, followed by wet etching of the YIG layer using phosphoric acid (H_3PO_4 85%) at 130°C . Spin-on carbon (SOC) was employed for planarization, followed by an additional deposition of 30 nm SiO_2 to enhance adhesion. Au antennas (200 nm thick, 5 μm wide) were subsequently defined using a lift-off process.³⁴

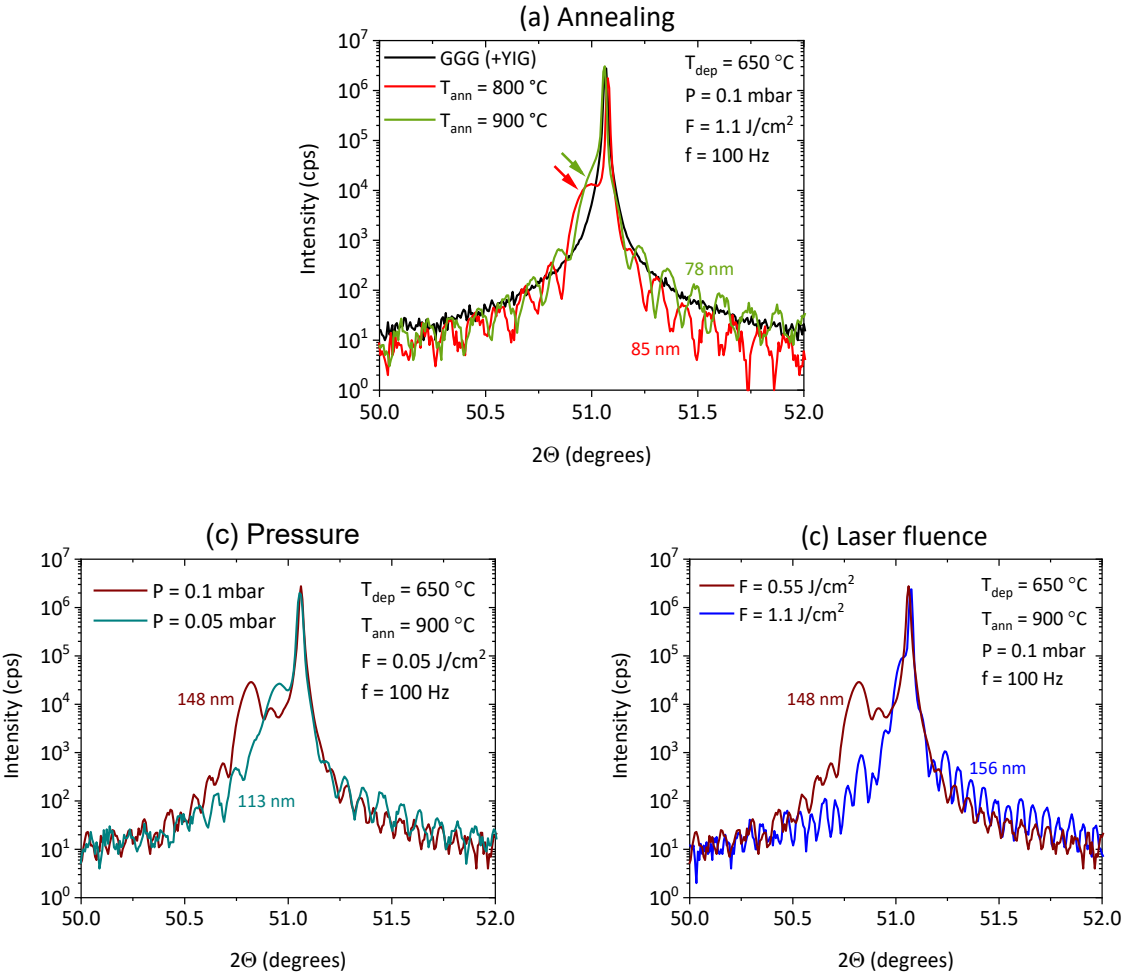
III. RESULTS AND DISCUSSION

A. Crystalline Structure

The crystallographic structure of the YIG films was investigated using X-ray diffraction analysis, with a focus on comparing films of similar thicknesses. YIG, a ferrimagnetic garnet with cubic lattice structure, exhibits epitaxial growth on isostructural GGG substrates with low defect densities due to the small lattice mismatch of $\Delta a/a \sim 6 \times 10^{-4}$.³⁵ The (111)-oriented GGG substrate displays a well-defined (444) diffraction peak at $2\theta = 51.1^\circ$ in the 2θ - ω scans [Fig. 1(a); black solid line]. Following YIG deposition, the XRD spectrum remained unchanged, indicating that the YIG film was x-ray amorphous. However, post-annealing resulted in the emergence of a shoulder at low 2θ in combination with distinct Laue oscillations in the diffraction pattern, which signifies the formation of a coherent crystalline YIG film.³⁶ These fringes were observed for both 800°C (red solid line) and 900°C (green solid line) post-deposition annealing temperatures in ultrathin YIG films with comparable

thicknesses (~80 nm). The shoulder could be attributed to the YIG (444) reflection with a slightly larger out-of-plane lattice parameter than bulk YIG and GGG.

A notable observation was the shift of the YIG (444) shoulder [indicated by arrows in Fig. 1(a)] towards the main GGG (444) peak upon increasing the annealing temperature to 900°C. This shift suggests a weaker tetragonal distortion of the YIG film—and thus lower residual strain—at higher annealing temperatures. While 800°C annealing yielded already high-quality epitaxial films, elevating the annealing temperature to 900°C further enhanced the epitaxial film quality. Consequently, 900°C was selected as the standard annealing temperature for the remainder of this study.



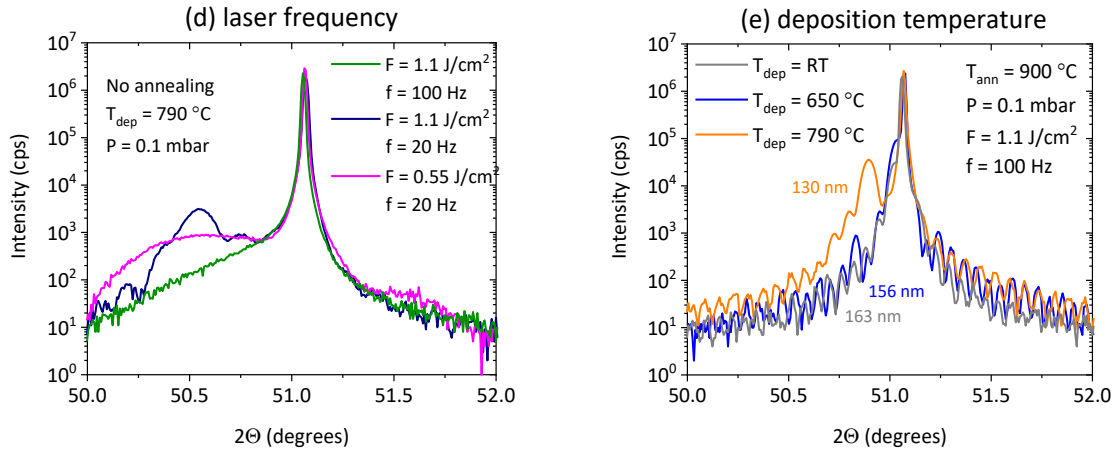


FIG. 1. Epitaxial YIG films on GGG substrates. High resolution – XRD spectra of YIG films. (a) GGG substrate for reference (black line), and YIG films after annealing at different temperatures at 800°C (red line), and 900°C (green line). (b) O₂ Pressure effect: depositions performed at 0.05 mbar (green line) and 0.1 mbar (brown line), after annealing (900°C). (c) Laser fluence effect: depositions performed at 0.55 J/cm² (brown line) and of 1.1 J/cm² (blue line), after annealing (900 °C). (d) Effect of low deposition rate: fluence of 1.1 J/cm² and frequency of 100 Hz (green line); 1.1 J/cm² and 20 Hz (dark blue line); and 0.55 J/cm² and 20 Hz (pink line). (e) Deposition temperature effect: YIG films deposited at RT (gray line), 650°C (blue line) and 790°C (orange line), after annealing (900°C).

Although post-deposition annealing is crucial for achieving high-quality epitaxial films, further investigations have revealed a substantial influence of various PLD deposition parameters on the properties of the annealed YIG films. For instance, Fig. 1(b) illustrates the impact of the PLD deposition pressure by contrasting two films grown under identical conditions except for O₂ pressure: 0.05 mbar (green line) and 0.1 mbar (brown line). We note that both films were subjected to identical post-deposition conditions.

It is well established that the O₂ pressure during deposition has a profound impact on the PLD growth mode, modifying both the ablation plume profile and the oxygen content within the growing film. Although some studies have reported advantages of higher deposition pressures up to 0.67 mbar for YIG PLD,²⁶ several studies in the literature suggest that lower pressures on the order of 0.01 - 0.05 mbar typically yield superior film quality.^{11,23,27} The data in Fig. 1(b) indicate that the O₂ pressure during PLD significantly affects the tetragonal distortion and the residual strain in the films, as evidenced by the shift of the YIG (444) reflection. This emphasizes that lower pressures are beneficial for enhancing film properties, a factor that becomes increasingly critical for thicker films, as will be demonstrated in the subsequent section.

A second critical deposition parameter in PLD of YIG is the laser fluence applied to the target. Laser fluence not only influences the deposition rate but also significantly impacts the profile of the ablated plume. Deposition

occurring at the plume edge, *i.e.*, closer to the substrate within the plume, generally results in more stoichiometric growth.³⁷ Outside the ablation plume, heavier atoms experience reduced scattering in the O ambient, leading to a less stoichiometric transfer.

Figure 1(c) presents a comparison of XRD spectra from YIG films deposited under identical conditions except for the laser fluence: 1.1 J/cm² (blue curve) and 0.55 J/cm² (brown curve). A significantly larger tetragonal distortion (*i.e.*, larger out-of-plane lattice parameter) can be deduced from the YIG (444) peak position for the lower fluence. This indicates that higher laser fluence promotes a more stoichiometric transfer from the target to the film, likely due to deposition occurring closer to the plume edge despite the higher deposition rate. Furthermore, a combined analysis of RBS and ERD revealed subtle variations in film stoichiometry. The calculated film compositions were determined to be Y_{3.7}Fe_{4.9}O_{11.3} for high fluence and Y_{3.7}Fe_{3.8}O_{12.5} for low fluence, with the stoichiometric composition being Y₃Fe₅O₁₂. These findings indicate that more stoichiometric iron transfer can be achieved with higher laser fluence. While different laser energies can also potentially influence the growth mode (*e.g.*, columnar growth), AFM analysis revealed a consistent surface roughness of 0.2 nm for both studied laser energies, suggesting a similar growth mode (data not shown). We note that this low surface roughness is crucial for minimizing magnetic damping within the YIG films.¹⁹

Although counterintuitive, post-deposition annealing is crucial for achieving epitaxial film growth despite the elevated deposition temperature. Film growth is characterized by dynamic surface processes involving continuous adatom diffusion and nucleation, whereas post-deposition annealing predominantly induces defect diffusion and atomic rearrangement within the film bulk. Thus, the deposition temperature alone does not fully replicate effects of post-deposition annealing. Potentially, epitaxial films could be obtained directly without annealing by employing significantly reduced deposition rates. Both laser fluence and frequency influence the deposition rate, but their effects differ fundamentally. Laser fluence directly modifies the ablation plume, impacting the film stoichiometry. Conversely, laser frequency modulates the temporal interval between successive plume bursts. At lower frequencies, adatoms have a longer time for thermalization and rearrangement before the arrival of the next plume, potentially facilitating improved epitaxial growth. However, strongly reduced deposition rates severely limit process throughput. Consequently, a balance must be found between deposition rate and post-deposition annealing to achieve optimal film quality and practical processing times.

This is illustrated in Fig. 1(d), which presents the XRD spectrum of an as-deposited YIG film grown at the maximum temperature of the PLD system (790°C) using a fluence of 1.1 J/cm² and a frequency of 100 Hz, the standard frequency employed in this study. Under these conditions, only the GGG (444) substrate peak is discernible in the XRD spectrum, indicative of an amorphous YIG film. Reducing the laser pulse frequency to 20 Hz (dark blue line) resulted indeed in the emergence of weak crystallinity within the as-deposited film. However, further decreasing the deposition rate by reducing the laser fluence (pink line) appeared to diminish the degree of crystallinity compared to the 20 Hz case. This observation aligns with the findings presented in Fig. 1(c), where higher laser fluences were shown to promote improved epitaxy. Despite exhibiting some degree of crystallinity, the epitaxial quality of these as-deposited films remained however low. Consequently, achieving high-quality YIG films without post-deposition annealing presents a significant challenge. Although prior substrate thermal treatment has shown some promise to improve this issue,^{16,30} it does not offer a substantial processing advantage compared to post-deposition annealing.

While the deposition temperature does not directly influence the stoichiometry or shape of the plasma plume, it significantly impacts the surface diffusion of impinging adatoms, as mentioned above, leading to variations in atomic arrangements within the growing film. This ultimately results in discernible differences in the crystallographic properties observed after post-deposition annealing. Figure 1(e) illustrates XRD spectra of YIG films deposited at different temperatures (790°C, 650°C, and room temperature (RT)) following identical post-deposition annealing. Epitaxial films were obtained for all deposition temperatures, albeit with distinct crystallographic characteristics. In particular, a larger tetragonal lattice distortion was observed for films deposited at 790°C.

One crucial factor contributing to the exceptional properties of YIG films grown on GGG substrates is the close lattice match between their respective lattice constants ($a_{\text{YIG}} = 12.376 \text{ \AA}$, $a_{\text{GGG}} = 12.383 \text{ \AA}$; $\Delta a/a \sim 6 \times 10^{-4}$). However, the differential thermal expansion coefficients of YIG and GGG likely contribute to a more pronounced lattice mismatch at the highest deposition temperature, resulting in increased residual strain within the film upon cooling.³⁸ In contrast, negligible crystallographic differences were observed between films deposited at RT and 650°C. However, as will be demonstrated later, the FMR signal intensity for the RT-deposited film is notably lower, suggesting incomplete crystallization within this film.

B. Scanning Transmission Electron Microscopy

A key finding of this study is the apparent discrepancy between the requirement for high-temperature annealing (900 °C) and the beneficial effect of intermediate deposition temperatures (optimal at 650 °C). To elucidate the underlying mechanisms, STEM analysis was conducted on films deposited at 650 °C and 790 °C following post-deposition annealing. For films deposited at 650 °C [Fig. 2(a)], imaging by STEM revealed a remarkably sharp interface between the YIG film and the GGG substrate, characterized by a perfect lattice match and an absence of interfacial dislocations. Furthermore, these films exhibited a near-perfect crystalline structure with minimal defects [Fig. 2(b)].

In contrast, films deposited at 790 °C contained localized defects within the YIG lattice [Fig. 2(c), blue arrows]. These defects, distinct from (threading) dislocations, do not extend to the interface and manifest as elongated regions with varying contrast. Combined atomic bright-field and cross-sectional STEM analysis suggests that these regions may represent areas with a higher concentration of light elements (possibly O) and potentially exhibit local variations in crystallographic structure. The reduced intensity of the atomic columns in bright-field imaging, compared to Z-contrast imaging, further supports the presence of local crystallographic variations (see Supplementary Material). These localized regions likely introduce strain within the film, contributing to the larger tetragonal distortion observed in the XRD spectra [Fig. 1(e)]. These findings clearly demonstrate that, despite the high-temperature annealing process, lower deposition temperatures (*i.e.*, 650 °C) yield significantly superior YIG film quality in terms of crystalline perfection and interfacial integrity.

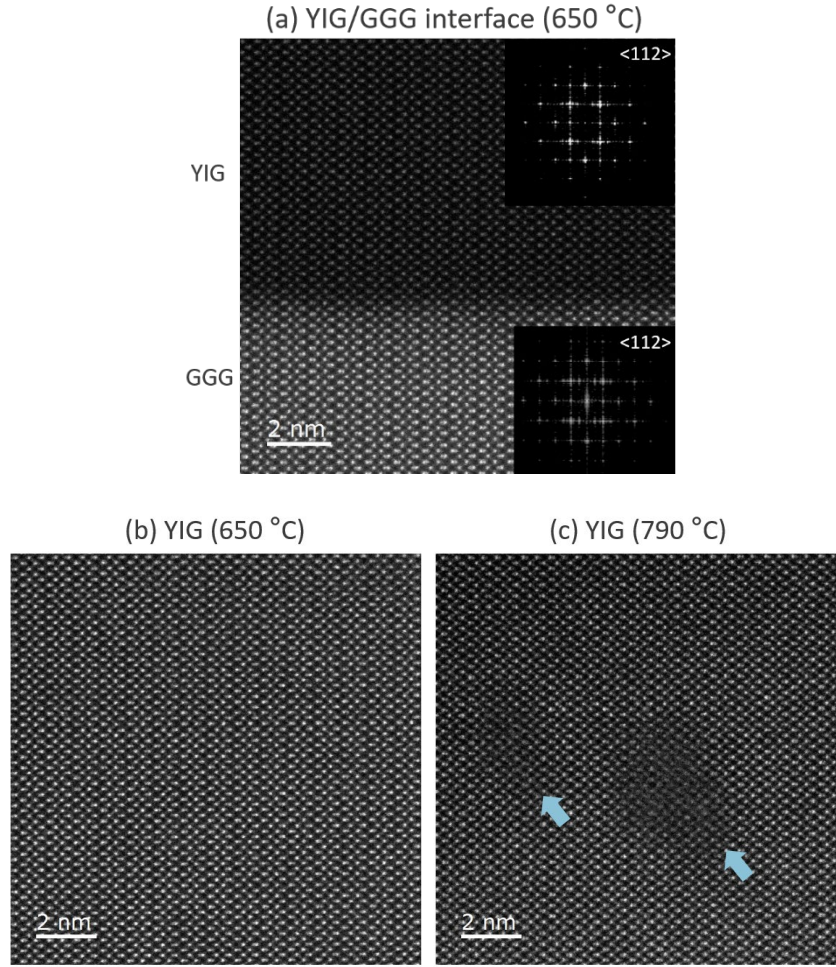


FIG. 2. High resolution STEM imaging. (a) YIG/GGG interface ($T_{\text{dep}} = 650 \text{ }^{\circ}\text{C}$), the insets show the selected area electron diffraction of YIG and GGG. YIG film detail for T_{dep} of (b) $650 \text{ }^{\circ}\text{C}$ and (c) $790 \text{ }^{\circ}\text{C}$, the blue arrows indicate the observed defects.

C. Ferromagnetic Resonance (FMR)

To correlate magnetic properties with the previously established structural characteristics, Vector Network Analyzer (VNA)-FMR measurements were performed to characterize the magnetic dynamics of the YIG films. The measured absorption spectra were fitted to a Lorentzian curve, which enables the extraction of key magnetic parameters such as the saturation magnetization (M_s) and magnetic damping (α) from the resonance frequency and linewidth, respectively.^{39,40}

The determination of ultralow Gilbert damping in state-of-the-art YIG films is inherently limited by the finite dimensions of the coplanar waveguide (CPW) used for the FMR measurements. As reported in Ref. ⁴¹ and detailed

in the Supplementary Information, the finite size of the CPW leads to a broadened emission spectrum, resulting in an apparent linewidth that is independent of the intrinsic film damping for values below approximately 3×10^{-4} (calculated for a 150 nm thick film at 6 GHz). While the FMR technique accurately resolves damping values characteristic of materials such as CoFeB or permalloy (NiFe) with $\alpha \sim 10^{-3}$, the resolution limit imposed by the CPW dimensions impedes the precise quantification of ultralow damping values characteristic of epitaxial YIG films with $\alpha \sim 10^{-4}$. To corroborate this limitation on the FMR damping resolution, measurements were performed using three independent FMR setups. Furthermore, repeated measurements (up to five times) on the same ultralow damping samples yielded a range of damping values between 0.3×10^{-4} and 2×10^{-4} , consistent with the estimated linewidth broadening due to the finite CPW dimensions ($< 3 \times 10^{-4}$). Based on these observations, a lower limit of 3×10^{-4} was adopted for the magnetic damping in this study.

By the FMR measurements, we could unequivocally establish a strong correlation between the epitaxial quality of YIG films (*cf.* Fig. 1) and their magnetic damping. Specifically, all samples exhibiting well-defined Laue fringes in XRD measurements demonstrated ultralow magnetic damping values ($< 3 \times 10^{-4}$), while those lacking such fringes showed negligible FMR signals. Furthermore, non-annealed samples deposited at a lower laser frequency (20 Hz), despite exhibiting some degree of crystallinity as evidenced in Fig. 1(d), exhibited significantly higher damping values of $\alpha = 0.004$ and 0.006 for fluences of 1.1 and 0.55 J/cm^2 , respectively. These values are comparable to those observed in materials such as CoFeB and permalloy ($\sim 10^{-3}$). The lower damping observed at higher fluence corroborates the findings presented in Fig. 1(c), which demonstrate the beneficial effects of higher fluence on film stoichiometry. This suggests that reducing the laser frequency can improve the film crystallinity up to a certain point, beyond which adatom thermalization becomes limited, ultimately hindering further improvement and reducing the deposition rate. In contrast, the laser fluence exhibits an optimal value that facilitates stoichiometric deposition at the plume edge, as previously discussed.³⁷

To further investigate the magnetic properties, we have also analyzed the FMR susceptibility, which is defined as:

$$\chi = \frac{\ln S_{11}}{\ln S_{11}^{Ref}} - 1,$$

where S_{11} is the microwave reflection S -parameter at a given magnetic bias field, and S_{11}^{Ref} the signal at zero applied magnetic field. This quantity directly correlates with the spin-wave transmission signal measured at the device level, as will be demonstrated below. Additionally, for films with similar magnetic moments, the peak

height can act as an indicator of the actual peak width, since the integrated signals should be comparable. Therefore, higher signals should correspond to narrower bandwidths, indicative of the frequency independent linewidth broadening (inhomogeneous broadening).

Figures 3(a)-(c) present comparative FMR data for samples deposited under varying conditions, mirroring the approach employed in Fig. 1. The FMR spectra were acquired within the 10 – 11 GHz frequency range under an out-of-plane magnetic field of 6500 Oe. A clear correlation emerges between the XRD analysis and the FMR signal intensity: closer YIG (444) and GGG (444) XRD peaks consistently correspond to a stronger FMR signal. This observed correlation holds true across all investigated deposition parameters, including laser fluence [Fig. 3(a)], O pressure [Fig. 3(b)], and deposition temperature [Fig. 3(c)].

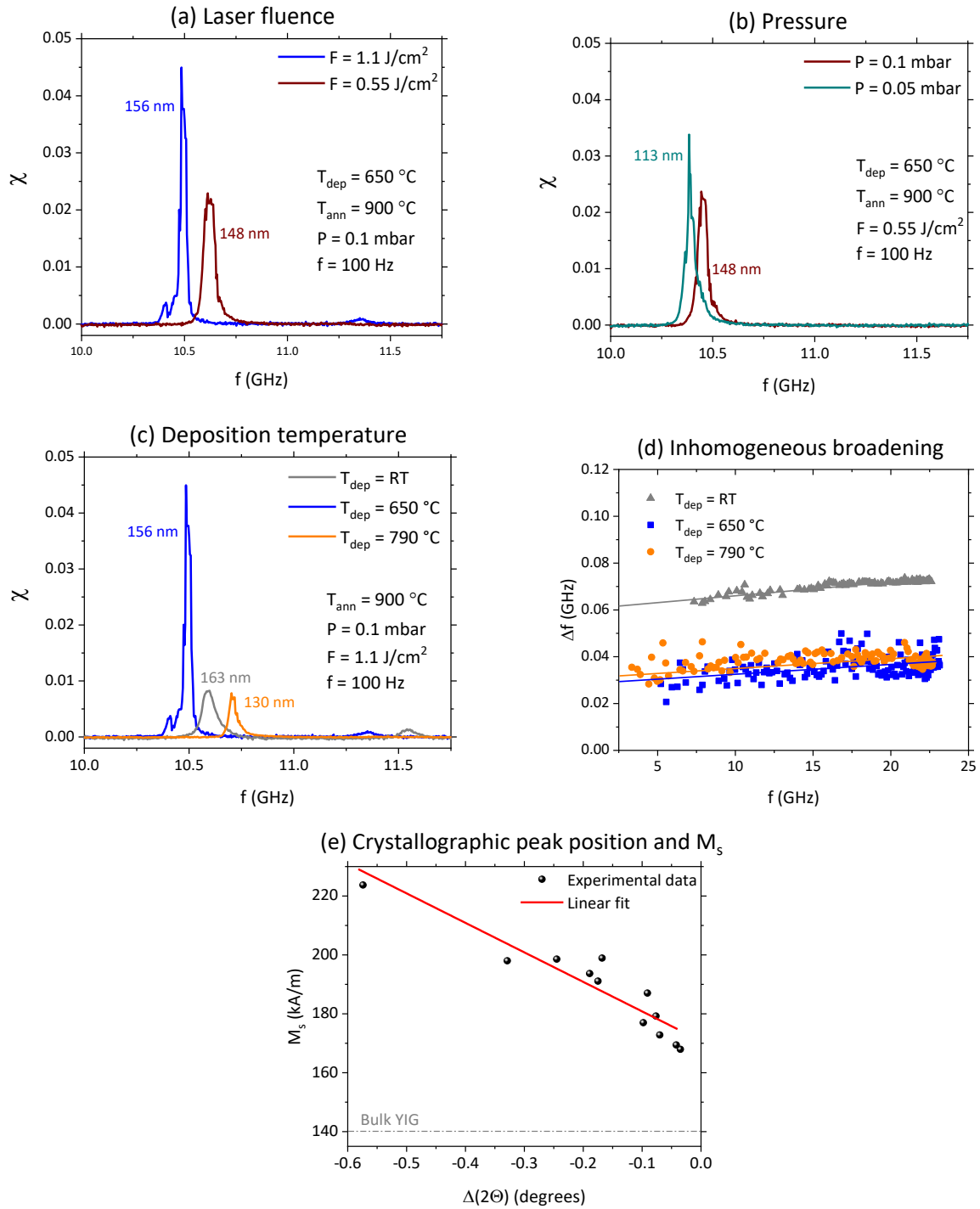


FIG. 3. FMR measurements of films deposited at different conditions. (a) Laser energy effect: deposition performed at a fluence of 1.1 J/cm^2 (blue line) and 0.55 J/cm^2 (brown line). (b) Pressure effect: deposition performed at an O_2 pressure of 0.1 mbar (brown line) and 0.05 mbar (green line). (c) Temperature effect: YIG films deposited at RT (gray line), 650°C (blue line) and 790°C (orange line). (d) FMR linewidth as a function of the frequency for the different temperature setpoints RT (gray triangles), 650°C (blue squares) and 790°C (orange circles). (e) Correlation between crystallographic and FMR data: M_s as a function of the distance between the YIG and GGG peak positions observed in the HR-XRD spectra.

It is important to note that the extracted damping values only reflect the frequency-dependent linewidth broadening (homogeneous broadening). In contrast, the magnon lifetime is intrinsically influenced by both homogeneous and inhomogeneous broadening mechanisms. Therefore, while low damping is a necessary condition for extended magnon lifetimes, it may not be a sufficient condition.

Figure 3(d) illustrates the linewidth (full width at half maximum, FWHM) as a function of frequency for films deposited at different temperatures, corresponding to the conditions in Fig. 3(c). Despite exhibiting similar intrinsic Gilbert damping values α , as determined from the slope of linewidth vs. frequency plots, the films displayed variations in inhomogeneous broadening (measured at $f = 0$). Notably, the film deposited at room temperature exhibited a higher degree of inhomogeneous broadening, suggesting shorter magnon lifetimes compared to films deposited at higher temperatures. Contrary to some previous reports,^{11,23} our findings indicate that deposition temperatures on the order of 650 °C yield superior film quality in terms of both low damping and minimized inhomogeneous broadening, ultimately leading to longer magnon lifetimes.

These results reveal a clear correlation between the crystallographic quality of the YIG films and their FMR behavior. Specifically, the degree of tetragonal distortion and residual strain, as evidenced by the separation between the YIG (444) and GGG (444) peaks in the XRD spectra (Fig. 1), emerges as a reliable indicator of the magnetic properties of the YIG films. While the precise quantification of ultralow damping values presents experimental challenges, as discussed above, and the comparison of FMR signal magnitudes is only practical for films of comparable thickness, the saturation magnetization M_s can also provide a valuable metric for assessing the magnetic quality of the films. An M_s value approaching the bulk magnetization of YIG of ~ 140 kA/m is indicative of a higher degree of magnetic order within the film, suggesting properties more closely resembling those of bulk YIG.

Figure 3(e) depicts the dependence of the saturation magnetization M_s on the angular separation between the YIG (444) and GGG (444) peaks in the XRD spectra. A strong correlation is observed, establishing a quantitative relationship between the crystallographic quality of the YIG films and their magnetic properties. These findings can provide a valuable tool for fine-tuning the growth conditions of YIG films for optimal spintronic device performance through the analysis of XRD data without the need of microwave FMR measurements. It is noteworthy that previous literature reports have not consistently demonstrated a clear correlation between

magnetization saturation and damping.³² This discrepancy may be attributed to the inherent limitations in accurately quantifying ultralow damping values, as discussed earlier.

D. YIG-based spin-wave transmission devices

Having established optimized deposition conditions ($T_{\text{dep}} = 650\text{ }^{\circ}\text{C}$, $F = 1.1\text{ J/cm}^2$, $f = 100\text{ Hz}$, $T_{\text{ann}} = 900\text{ }^{\circ}\text{C}$, $P = 0.1\text{ mbar}$), we proceeded to deposit thicker YIG films. This facilitates subsequent device-level characterization due to the enhanced magnetic signal. Figures 4(a) and 4(b) present reciprocal space maps (RSMs) of YIG films grown under these conditions with thicknesses of 156 nm and 637 nm, respectively. These RSM measurements corroborate the HR-XRD analysis in Fig. 1, offering further insights into the film's crystallographic orientation.

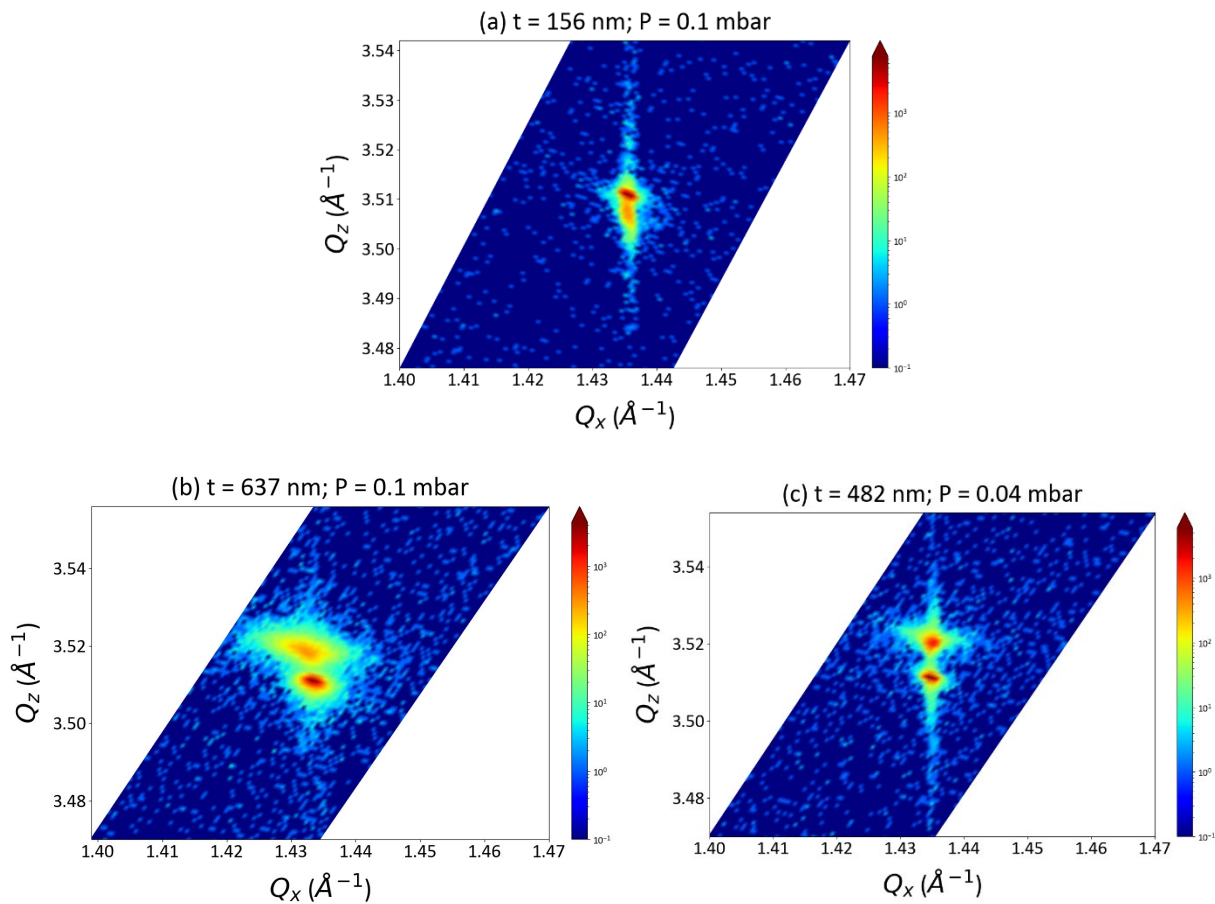
A notable observation is that the YIG peak exhibits a thickness-dependent shift in reciprocal space, crossing the GGG substrate peak position. This indicates that the out-of-plane lattice constant of YIG is initially larger than that of GGG in thin films, resulting in tensile out-of-plane strain. However, as the YIG film thickness increases, the lattice constant of YIG decreases, leading to compressive out-of-plane strain. This indicates that the out-of-plane lattice constant of YIG is larger than GGG for thin YIG films, while it becomes smaller than that of GGG for thicker films. Consequently, the film transitions from extended to compressed in the vertical direction. exhibits increased broadness and tilting along the horizontal direction, suggesting the presence of considerable non-tetragonal distortion and an elongation of the lattice constant along the horizontal direction.

Furthermore, the RSMs of thicker films exhibit increased peak broadening and tilting along the horizontal direction. This suggests the presence of substantial non-tetragonal distortion and an elongation of the in-plane lattice constant. Considering the expected lattice constants of YIG (12.376 \AA) and GGG (12.383 \AA), the observed in-plane lattice expansion clearly indicates a lattice mismatch between the film and the substrate, possibly due to an increased defect density within the thicker films.

Based on the preceding analysis, a reduced O_2 pressure is preferred for improved epitaxial film quality. Figure 4(c) presents the RSM of a thicker YIG film (482 nm) deposited under the same conditions as before, except with a lower oxygen pressure of 0.04 mbar. In contrast to the previous results, this film exhibits fully strained, pseudomorphic growth. However, the YIG peak remains shifted to the opposite side of the GGG peak compared

to the thinner films. This observation underscores the significant impact of film thickness on the YIG lattice constant, leading to either a compressive or tensile strain state.

While numerous studies on PLD have investigated YIG films with nm thicknesses,^{11,14,16,19,20,24} the pronounced influence of film thickness on the resulting YIG properties has not been previously reported. Our findings demonstrate that PLD is particularly well-suited for the deposition of thin YIG films, including those in the sub-micrometer range, while LPE may be more advantageous for applications requiring thicker films.³⁴ However, by optimizing the PLD deposition parameters, it is possible to achieve high-quality YIG films with thicknesses exceeding the micrometer range.^{31,42}



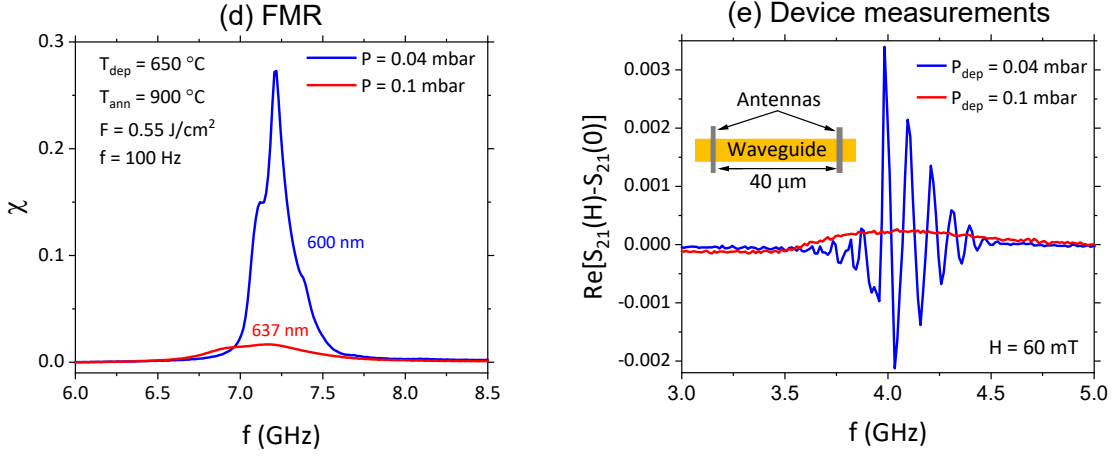


FIG. 4. Material properties and measurements at device level. RSMs measured for (a) $t = 156$ nm and $P = 0.1$ mbar; (b). $t = 637$ nm and $P = 0.1$ mbar; and (c) $t = 482$ nm and $P = 0.04$ mbar. The other used parameters were: $T_{\text{dep}} = 650$ °C, $F = 1.1$ J/cm², $f = 100$ Hz and $T_{\text{ann}} = 900$ °C. (d) FMR and (e) measurements at device level for the thicker films deposited at 0.04 mbar (blue curve) and 0.1 mbar (red curve). The inset of (e) shows a schematic representation of the fabricated device.

The crystallographic quality of the films profoundly influences their magnetic properties. Figure 4(d) presents FMR spectra of the two thick YIG films deposited at different O₂ pressures: 0.1 mbar (red line) and 0.04 mbar (blue line). The pseudomorphic film deposited at the lower pressure exhibits a significantly higher and sharper FMR signal, despite its smaller thickness. However, the presence of multimode precession around the main resonance peak suggests a more pronounced granular structure within the thicker film. This multimode precession precluded a reliable Lorentzian fit to the FMR data, preventing the accurate determination of the Gilbert damping parameter α and saturation magnetization M_s .

Both sets of deposition conditions, utilizing thicker YIG films, were employed for the fabrication of spin-wave transmission devices. The fabricated devices consisted of a 15 μm wide YIG spin-wave waveguide and two inductive antennas separated by 40 μm [inset of Fig. 4(e)]. Two distinct signal propagation behaviors were observed for devices fabricated using YIG films grown under the two different pressure conditions [Fig. 4(e)].

The device fabricated using the YIG film grown at 0.04 mbar exhibited a substantially larger signal amplitude, consistent with the enhanced FMR response observed for this film. Furthermore, clear phase oscillations were observed in the signal transmitted through this device, a well-established hallmark of spin-wave propagation, indicating efficient device performance. In contrast, only incoherent precession was observed in the device fabricated using the YIG film grown at 0.1 mbar.

These findings demonstrate a strong correlation between the material properties of the YIG films, including their crystallographic quality and magnetic properties, and the resulting device functionality. Coherent spin wave propagation was observed over distances as large as 115 μm (the maximum fabricated distance) in the device fabricated using the high-quality, low-pressure grown YIG film. We note that despite the observation of multi-mode FMR signals in the bulk material, a clear, apparently single-mode signal was measured in the spin-wave transmission devices. This suggests that the multi-mode behavior observed in the FMR measurements may originate from magnetic inhomogeneities on larger scales, which have negligible impact on spin-wave propagation within the micrometer-sized devices.

IV. CONCLUSIONS

In conclusion, we have demonstrated a strong correlation between the crystallographic YIG (444) peak position, readily assessable via HR-XRD, and the bulk magnetic properties and subsequent spin-wave propagation. These findings offer a promising approach for the rapid and simplified assessment of YIG film quality, potentially obviating the need for more complex and costly characterization techniques such as vector network analyzer ferromagnetic resonance.

Furthermore, this work provides a comprehensive overview of optimized PLD parameters for the growth of state-of-the-art YIG films. These optimized conditions (fluence of 1.1 J/cm^2 , deposition pressure of 0.04 mbar, deposition temperature of 650 $^{\circ}\text{C}$, and annealing temperature of 900 $^{\circ}\text{C}$) yield epitaxial films with minimal defects and exhibit ultralow magnetic damping ($\alpha < 3 \times 10^{-4}$).

This study also sheds light on the impact of film thickness on the properties of PLD-grown YIG films, highlighting the inherent scalability advantages of PLD for the fabrication of devices utilizing sub- μm thick YIG films. The optimized deposition parameters, validated through device-level measurements, provide a robust foundation for the future development of high-performance YIG-based spintronic devices.

ACKNOWLEDGEMENTS

J.D.C. acknowledges financial support from the European Union MSCA-IF Neuromag under Grant Agreement No. 793346. FC's and CA's contributions have been funded in part by the European Union's Horizon 2020 research and innovation program within the FET-OPEN project CHIRON under grant agreement No. 801055. The authors would like to thank Sean McMitchell for fruitful discussions.

REFERENCES

1. Chumak, A. V., Vasyuchka, V. I., Serga, A. A. & Hillebrands, B. Magnon spintronics. *Nat Phys* **11**, 453–461 (2015).
2. Fischer, T. *et al.* Experimental prototype of a spin-wave majority gate. *Appl Phys Lett* **110**, 152401 (2017).
3. Ciubotaru, F., Devolder, T., Manfrini, M., Adelmann, C. & Radu, I. P. All electrical propagating spin wave spectroscopy with broadband wavevector capability. *Appl Phys Lett* **109**, (2017).
4. Talmelli, G. *et al.* Spin-Wave Emission by Spin-Orbit-Torque Antennas. *Phys. Rev. Applied* **10**, 44060 (2018).
5. Dubs, C. *et al.* Sub-micrometer yttrium iron garnet LPE films with low ferromagnetic resonance losses. *J Phys D Appl Phys* **50**, 204005 (2017).
6. Pirro, P. *et al.* Spin-wave excitation and propagation in microstructured waveguides of yttrium iron garnet / Pt bilayers. *Appl Phys Lett* **104**, 1–5 (2014).
7. Yang, Q. *et al.* Effects of off-stoichiometry and density on the magnetic and magneto-optical properties of yttrium iron garnet films by magnetron sputtering method. *J Appl Phys* **108**, (2010).
8. Liu, T. *et al.* Ferromagnetic resonance of sputtered yttrium iron garnet nanometer films. *J Appl Phys* **115**, 2–5 (2014).
9. Lustikova, J. *et al.* Spin current generation from sputtered Y₃Fe₅O₁₂ films. *J Appl Phys* **116**, (2014).
10. Li, Z. *et al.* Magnetization dynamics in the YIG/Au/YIG magnon valve. *APL Mater* **10**, (2022).
11. Hauser, C. *et al.* Yttrium Iron Garnet Thin Films with Very Low Damping Obtained by Recrystallization of Amorphous Material. *Sci Rep* **6**, 20827 (2016).
12. Onbasli, M. C. *et al.* Pulsed laser deposition of epitaxial yttrium iron garnet films with low Gilbert damping and bulk-like magnetization. *APL Mater* **2**, (2014).
13. Jungfleisch, M. B. *et al.* Spin waves in micro-structured yttrium iron garnet nanometer-thick films. *J Appl Phys* **117**, (2015).

14. Qin, H., Hämäläinen, S. J., Arjas, K., Witteveen, J. & van Dijken, S. Propagating spin waves in nanometer-thick yttrium iron garnet films: Dependence on wave vector, magnetic field strength, and angle. *Phys Rev B* **98**, (2018).
15. Collet, M. *et al.* Spin-wave propagation in ultra-thin YIG based waveguides. *Appl Phys Lett* **110**, 92408 (2017).
16. Kelly, O. d'Allivy *et al.* Inverse spin Hall effect in nanometer-thick yttrium iron garnet / Pt system. *Appl Phys Lett* **103**, (2013).
17. Hahn, C. *et al.* Measurement of the intrinsic damping constant in individual nanodisks. *Appl Phys Lett* **104**, (2014).
18. Collet, M. *et al.* Spin Seebeck effect in nanometer-thick YIG micro-fabricated strips. *AIP Adv* **7**, (2017).
19. Sun, Y. *et al.* Growth and ferromagnetic resonance properties of nanometer-thick yttrium iron garnet films. *Appl Phys Lett* **101**, (2012).
20. Howe, B. M. *et al.* Pseudomorphic Yttrium Iron Garnet Thin Films With Low Damping and Inhomogeneous Linewidth Broadening. *IEEE Magn Lett* **6**, 2013–2016 (2015).
21. McMitchell, S. R. C. Research Update : New possibilities for the nanoscale engineering of complex oxide thin films. *APL Mater* **3**, (2015).
22. Willmott, P. R. & Huber, J. R. Pulsed laser vaporization and deposition. *Rev Mod Phys* **72**, 315–328 (2000).
23. Hauser, C. *et al.* Annealing of amorphous yttrium iron garnet thin films in argon atmosphere. *J Appl Phys* **122**, (2017).
24. Onbasli, M. C. *et al.* Pulsed laser deposition of epitaxial yttrium iron garnet films with low Gilbert damping and bulk-like magnetization. *APL Mater* **2**, 106102 (2014).
25. Sposito, A., Stenning, G. B. G., Groot, P. A. J. De & Eason, R. W. Pulsed laser deposition of high-quality μ m-thick YIG films on YAG. *Opt Mater Express* **3**, 77–85 (2013).
26. Zaki, A. M., Blythe, H. J., Heald, S. M., Fox, A. M. & Gehring, G. A. Growth of high quality yttrium iron garnet films using standard pulsed laser deposition technique. *J Magn Magn Mater* **453**, 254–257 (2018).
27. Jin, L. *et al.* Pulsed laser deposition grown yttrium-iron-garnet thin films: Effect of composition and iron ion valences on microstructure and magnetic properties. *Appl Surf Sci* **483**, 947–952 (2019).
28. Li, S. *et al.* Epitaxial patterning of nanometer-thick Y₃Fe₅O₁₂ films with low magnetic damping. *Nanoscale* **8**, 388–394 (2016).
29. Jungfleisch, M. B. *et al.* Insulating Nanomagnets Driven by Spin Torque. *Nano Lett* **17**, 8–14 (2017).
30. Tang, C. *et al.* Exquisite growth control and magnetic properties of yttrium iron garnet thin films. *Appl Phys Lett* **108**, (2016).
31. Dorsey, P. C. *et al.* Epitaxial yttrium iron garnet films grown by pulsed laser deposition. *J Appl Phys* **74**, (1993).

32. Schmidt, G., Hauser, C., Trempler, P., Paleschke, M. & Papaioannou, E. T. Ultra Thin Films of Yttrium Iron Garnet with Very Low Damping : A Review. *Physica Status Solidi B* **1900644**, (2020).
33. Blank, D. H. A., Dekkers, M. & Rijnders, G. Pulsed laser deposition in Twente: from research tool towards industrial deposition. *J Phys D Appl Phys* **47**, 34006 (2014).
34. Costa, J. D. *et al.* Compact tunable YIG-based RF resonators. *Appl Phys Lett* **118**, (2021).
35. Mallmann, E. J. J., Sombra, A. S. B., Goes, J. C. & Fechine, P. B. A. Yttrium Iron Garnet: Properties and Applications Review. *Solid State Phenomena* **202**, 65–96 (2013).
36. Triscone, J. M., Fivat, P., Andersson, M., Decroux, M. & Fischer, O. Two-dimensional and three-dimensional vortex lattice dynamics in DyBa₂Cu₃O₇-(Y_{1-x}Pr_x)Ba₂Cu₃O₇ coupled heterostructures. *Phys Rev B* **50**, 1229–1236 (1994).
37. Proyer, S. & Stangl, E. Time-integrated photography of laser-induced plasma plumes. *Appl Phys A Mater Sci Process* **60**, 573–580 (1995).
38. Rodic, D., Szytula, A., Tomkowicz, Z., Guillot, M. & Le Gall, H. Temperature dependence of lattice constants and thermal expansion coefficient of terbium-yttrium ferrites garnets. *J Magn Magn Mater* **75**, 79–87 (1988).
39. Tamaru, S., Tsunegi, S., Kubota, H. & Yuasa, S. Vector network analyzer ferromagnetic resonance spectrometer with field differential detection. *Review of Scientific Instruments* **89**, (2018).
40. Devolder, T. Using rf voltage induced ferromagnetic resonance to study the spin-wave density of states and the Gilbert damping in perpendicularly magnetized disks. *Phys Rev B* **104413**, 1–11 (2017).
41. Sushruth, M. *et al.* Electrical spectroscopy of forward volume spin waves in perpendicularly magnetized materials. *Phys Rev Res* **2**, (2020).
42. Manuilov, S. A., Fors, R., Khartsev, S. I. & Grishin, A. M. Submicron Y₃Fe₅O₁₂ Film Magnetostatic Wave Band Pass Filters. *J Appl Phys* **105**, (2009).